sensors

MDPI

Article

Design and Simulation Investigation of Si_3N_4 Photonics Circuits for Wideband On-Chip Optical Gas Sensing around 2 μm Optical Wavelength

Natnicha Koompai [1,2], Papichaya Chaisakul [2,*], Pichet Limsuwan [3], Xavier Le Roux [1], Laurent Vivien [1] and Delphine Marris-Morini [1]

1 Centre de Nanosciences et de Nanotechnologies, Université Paris Sud, CNRS, Université Paris Saclay, 91120 Palaiseau, France; natnicha.koompai@u-psud.fr (N.K.); xavier.leroux@u-psud.fr (X.L.R.); laurent.vivien@c2n.upsaclay.fr (L.V.); delphine.morini@u-psud.fr (D.M.-M.)
2 Department of Physics, Faculty of Science, Kasetsart University, Bangkok 10900, Thailand
3 Department of Physics, Faculty of Science, King Mongkut's Institute of Technology Ladkrabang, Bangkok 10520, Thailand; pichet.li@kmitl.ac.th
* Correspondence: fscipac@ku.ac.th

Abstract: We theoretically explore the potential of Si_3N_4 on SiO_2 waveguide platform toward a wideband spectroscopic detection around the optical wavelength of 2 μm. The design of Si_3N_4 on SiO_2 waveguide architectures consisting of a Si_3N_4 slot waveguide for a wideband on-chip spectroscopic sensing around 2 μm, and a Si_3N_4 multi-mode interferometer (MMI)-based coupler for light coupling from classical strip waveguide into the identified Si_3N_4 slot waveguides over a wide spectral range are investigated. We found that a Si_3N_4 on SiO_2 slot waveguide structure can be designed for using as optical interaction part over a spectral range of interest, and the MMI structure can be used to enable broadband optical coupling from a strip to the slot waveguide for wideband multi-gas on-chip spectroscopic sensing. Reasons for the operating spectral range of the system are discussed.

Keywords: Si_3N_4 on SiO_2; multi-mode interferometer; short-wave infrared

Citation: Koompai, N.; Chaisakul, P.; Limsuwan, P.; Le Roux, X.; Vivien, L.; Marris-Morini, D. Design and Simulation Investigation of Si_3N_4 Photonics Circuits for Wideband On-Chip Optical Gas Sensing around 2 μm Optical Wavelength. *Sensors* **2021**, *21*, 2513. https://doi.org/10.3390/s21072513

Academic Editors: Ashim Dhakal and Vittorio M. N. Passaro

Received: 15 February 2021
Accepted: 1 April 2021
Published: 3 April 2021

1. Introduction

Photonic integration on silicon (Si) offers a unique opportunity in optical communication, sensing, and spectroscopic applications [1–4]. For the latter, interaction between evanescent field around Si-based optical waveguide and gas molecules enables the absorption spectrum of sensed gas molecules to be measured in millimeter-sized chips [5–7]. With an additional advantage of on-chip integration with Si electronic circuits, Si-based integrated spectroscopic sensing could provide substantial benefits in terms of low cost, small footprint, low power, limited space employment, access to advanced noise reduction, and Si-CMOS high-volume manufacturing [8–12]. Several environmentally-important gas molecules have characteristic absorption lines within the short-wave infrared (~1.4–3 μm), mid-wave infrared (~3–8 μm), or long-wave infrared (~8–14 μm) [13,14]. On the one hand, a number of waveguide platforms have been experimentally or theoretically proposed, such as pedestal Si [15], chalcogenide-based waveguides [16,17], Si-on-sapphire [18], Ge-rich SiGe [19–21], and Si-on-Si_3N_4 waveguides [22], in order to take advantage of fingerprint absorption in the mid- and long-wave infrared regions. On the other hand, the short-wave infrared regions have also attracted significant attention despite having a weaker overtone absorption [23]. Spectroscopic detection around the ~1.6 μm wavelength range has been promisingly reported when detection at ppmv levels is desirable for a CH_4 detection using Si waveguide [8], in which conventional optical telecommunication components can be conveniently employed. For the ~2 μm wavelength range, besides its potential for optical communication [23,24], several important gases also have sufficiently strong

absorption bands in such wavelength ranges with sensing applications in environmental and process controls such as H_2O, NH_3, and CO_2 [25]. In comparison with the longer wavelength regions, photonic components in the short-wave infrared could be advantageous for the development of low-cost sensors and detectors without cooling [26–28]. Recent research investigation has included on-chip room-temperature optical sources and optical detection around ~2 μm wavelength ranges based on heterogeneous integration of III-V semiconductors on silicon such as GeSn [29–31], InP [32], strained InGaAs [33,34], or GaSb [23,27].

On the other hand, for the optical interaction part with sensed molecules, Si_3N_4 on SiO_2 waveguide platform is one of the Si-compatible platforms suitable for spectroscopic sensing in the short-wave infrared region. Si_3N_4 has a relatively large transparent window for the optical wavelength from 0.4 to 5 μm [26,35] and the optical absorption of SiO_2 increases noticeably at the optical wavelength larger than 3 μm [15,36]. Moreover, due to a moderate refractive index contrast between Si_3N_4 waveguide core (n ~ 2) and SiO_2 cladding (n ~ 1.45), as well as a wider bandgap than that of Si, the Si_3N_4/SiO_2 waveguide platform is also considered to be advantageous in terms of fabrication tolerance and wideband operation, as well as a high optical power handling capability [37]. Additionally, supercontinuum generation has been demonstrated from 1.2 to 3.7 μm spectral range from Si_3N_4 waveguides, increasing its suitability for spectroscopic sensing with the promising broadband coherent source in the short-wave infrared region [38].

In this paper, to explore the potential of Si_3N_4 on SiO_2 waveguide platform toward a wideband and simultaneous detection around 2 μm wavelength range, we report on the design of a Si_3N_4 on SiO_2 waveguide architecture that can be simultaneously employed for a wideband on-chip spectroscopic sensing around the 2 μm wavelength region using finite difference eigenmode (FDE) analysis [39] and eigenmode expansion (EME) method (Lumerical Inc.) [40,41]. Firstly, from systematic FDE simulation, we identify a Si_3N_4 slot waveguide that is suitable for wideband evanescent sensing around 2 μm optical wavelength. Subsequently, from the EME analysis, a Si_3N_4 multi-mode interferometer (MMI) with tapering slot waveguide is interestingly shown to enable simultaneous coupling of light over a spectral range into the identified Si_3N_4 slot waveguide for wideband on-chip optical gas sensing, coinciding with the absorption bands of several important gas molecules. From the analysis, we found that over a certain wavelength of interest, a particular slot waveguide structure can be designed for using as optical interaction part, and MMI structure can be employed to enable broadband optical coupling from strip to the slot waveguide for wideband multi-gas on-chip spectroscopic sensing.

2. Structure under Investigation: Si_3N_4 Multi-Mode Interferometer and Slot Waveguide

As shown in Figure 1, the structure under investigation consists of a Si_3N_4 multi-mode interferometer (MMI), tapering slot waveguides, and a slot waveguide. We aim to investigate the possibility to employ such structure for spectroscopic sensing over a wide spectral range around 2 μm wavelength region. The MMI part is used to efficiently couple light from a strip (or rib) waveguide, which can be used to generate or propagate light from the optical source, to a slot waveguide, i.e., the functional region of the sensor. The MMI devices are selected because of its potential for wideband operation and good fabrication tolerance [40]. For increasing optical interaction with the gas molecules, we focus our effort on slot waveguide structures because of its high light–matter interaction potentials [42,43]. It is worth noting that an MMI coupler is required because of the optical mode mismatch between the Gaussian-like mode of the strip waveguide and the non-Gaussian-like mode of the slot one [44]. To thoroughly evaluate the structure for wideband usage, several parameters of the MMI devices with the tapering slot parts and the slot waveguide should be systematically considered, as indicated in Figure 1, including the width of MMI entrance (w_{in}) and output (w_{out}) waveguides, the width of MMI main waveguide (w_{mmi}), the length of MMI main waveguide (L_{mmi}), the distance between the two output waveguides (D), the length of different tapering slot parts ($L_{out,1}$, $L_{out,2}$, and L_{taper}) between the MMI device

and the slot waveguide, the width of a two-side waveguide (w_{slot}) and the width of the slot gap (G_{slot}) of the slot waveguide, the total height of the Si_3N_4 layer (H), and the slab thickness (h). As H is the total Si_3N_4 waveguide thickness, if h is not equivalent to zero, the Si_3N_4 waveguide will not be etched down to SiO_2 substrate.

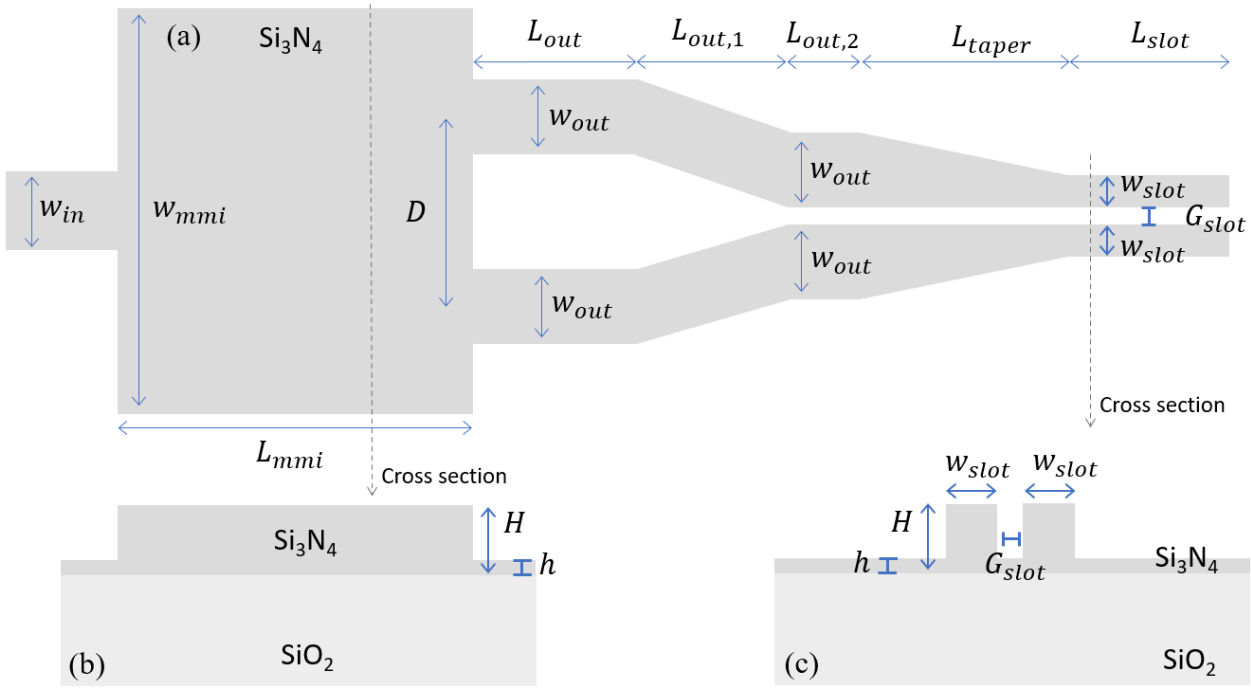

Figure 1. (**a**) Top view and (**b**,**c**) cross-sections of the structure under investigation consist of a Si_3N_4 multi-mode interferometer (MMI), tapering slot waveguides, and a slot waveguide with several parameters systematically considered in this work.

3. Slot Waveguides

Firstly, we focus on the slot waveguide structure that is suitable for a wideband usage around the 2 μm wavelength range. As the part of optical field which is not confined in the waveguide materials would interact with the gas molecule in the air, the ratio of the optical power in the air to the total guided optical power, $\eta = \iint_{air} P_z dxdy / \iint_{total} P_z dxdy$, can be used to potentially indicate the strength of light–gas interaction, in which P_z is the Poynting vector along the propagation direction [17,39]. Figure 2a–d report η for the slot waveguide with different H, h, G_{slot}, w_{slot}, and optical wavelength (λ) values from λ = 1.6 to 2.4 μm obtained from FDE analysis. As in Figure 2a, the values of η generally increase with higher values of waveguide height H, while the values of h, G_{slot}, and w_{slot} are kept constant at 0, 0.2, and 0.6 μm, respectively. At higher values of H, there is larger area of air gap in the slot waveguide available for optical field as in the inset of Figure 2a for λ = 2 μm. Nevertheless, for the shortest λ of 1.6 μm, the values of η slightly decrease at higher values of slot height H because part of the optical field starts to leak into the two-side waveguides of the slot due to its shorter wavelength values. Therefore, increasing H would instead decrease the fraction of optical power residing in the air, as also shown in the lowest right inset of Figure 2a. To obtain the best overall performance within the spectral range of interest that is compatible with typical fabrication constraints of nowadays high-quality Si_3N_4 deposition [45,46], the value of H is restricted to 1 μm in further simulation investigation. For slab thickness h, as in Figure 2b, the values of η generally increase with lower values of h, while the values of H, G_{slot}, and w_{slot} are kept constant at 1, 0.2, and 0.6 μm, respectively. This is because more optical field can be resided in the slab part of the waveguide as slab thickness values increase, as in the inset of Figure 2b. However, for λ = 2.4 μm, slab thickness h of 0.1 μm results in the better values of η because the slab

layer helps alleviate the leakage of the optical mode into the SiO_2 substrate for a relatively large wavelength value, as in the lowest right inset. For slot gap G_{slot}, as in Figure 2c, the values of η generally decrease with higher values of G_{slot}, while the values of H, h, and w_{slot} are kept constant at 1, 0, and 0.6 μm, respectively. G_{slot} of 0.2 μm appears to render the better overall values of η for λ from 1.6 to 2.4 μm. The values of slot gap G_{slot} need to be comparable to the exponential decay length of the fundamental guided mode [47]. For width of a two-side waveguide w_{slot}, when the values of H, h, and G_{slot} are respectively kept constant at 1, 0, and 0.2 μm, as in Figure 2d, light at different λ values show different optimized value of w_{slot}. Nevertheless, best compromised values of ~0.6 μm could be visibly indicated for w_{slot}. A slightly different optimized value of w_{slot} for each optical wavelength is due to the fact that for a given λ value, too small w_{slot} (respectively (resp.) too large w_{slot}) would lead to higher leakage into the SiO_2 substrate (resp. the two-side waveguide part), as illustrated in the inset of Figure 2d for λ of 2 μm. From the optical mode analysis demonstrated in Figure 2a–d in this paper, Si_3N_4 slot waveguide structure with H = 1 μm, h = 0 μm, G_{slot} = 0.2 μm, and w_{slot} = 0.6 μm is selected for potential wideband optical sensing considering both the overall η values and practical fabrication constraint of high quality Si_3N_4. Besides the η values, $\Gamma = \partial n_{mode}/\partial n_{air\ surrounding}$, when n_{mode} represents effective index of the guided optical mode, can also be used to express the sensitivity of waveguide with respect to the change in the surrounding refractive index, $n_{air\ surrounding}$. Γ was employed to compare different waveguide-based structures for traced gas sensing by spectroscopic absorption [48,49]. Figure 3a summarizes the values of η and Γ of the identified Si_3N_4 slot waveguide structure. Respectable values of Γ ~ 30% over a wide spectral range are obtained, comparable to the state-of-the-art devices designed to work at a particular wavelength value of ~1.64 and ~4.24 μm [8,49,50]. To explain the decreasing values of η and Γ at the shorter and longer optical wavelengths, Figure 3b–j show optical intensity of the quasi transverse-electric (TE) fundamental mode of the Si_3N_4 slot waveguide from λ = 1.6 to 2.4 μm. At the shorter (resp. longer) optical wavelength regions, optical mode intensity profiles of the first quasi-TE mode become progressively larger in the two-side waveguide parts (resp. SiO_2 substrate). Therefore, different optical mode profiles at different λ values would play an important role in dictating the spectral range in which a Si_3N_4 slot waveguide structure can be employed for optical sensing with good values of η and Γ. In the inset of Figure 3b–j, 3D mode profiles (Optiwave, 32-bit FDTD) of the electric field amplitude are also provided for every corresponding cross-sectional mode profile of optical intensity. The 3D mode profiles of the electric field are excellently agreeable with the cross-sectional one. At the shorter optical wavelengths, optical field of the quasi-TE mode is larger in the two-side waveguide parts. Then, the field is progressively shifted toward the center part of the slot waveguide; nevertheless, from the 3D view it might be more challenging to observe the slight shift of the optical field (the evanescent field) leaked into the substrate at the longer optical wavelengths. As the two data are supportive, we report both cross-sectional and 3D mode profiles. Last, but not least, it is important to note that a vertical slot waveguide will be required to have a smooth etched sidewall to avoid scattering loss due to the sidewall roughness [51]. Fabrication technology already allows smooth etched sidewalls in Si-based slot waveguide recording < 2 dB/cm propagation loss [52,53], and fabrication techniques to achieve micron-scale silicon nitride rib waveguide structure with smooth sidewall are promisingly reported [54].

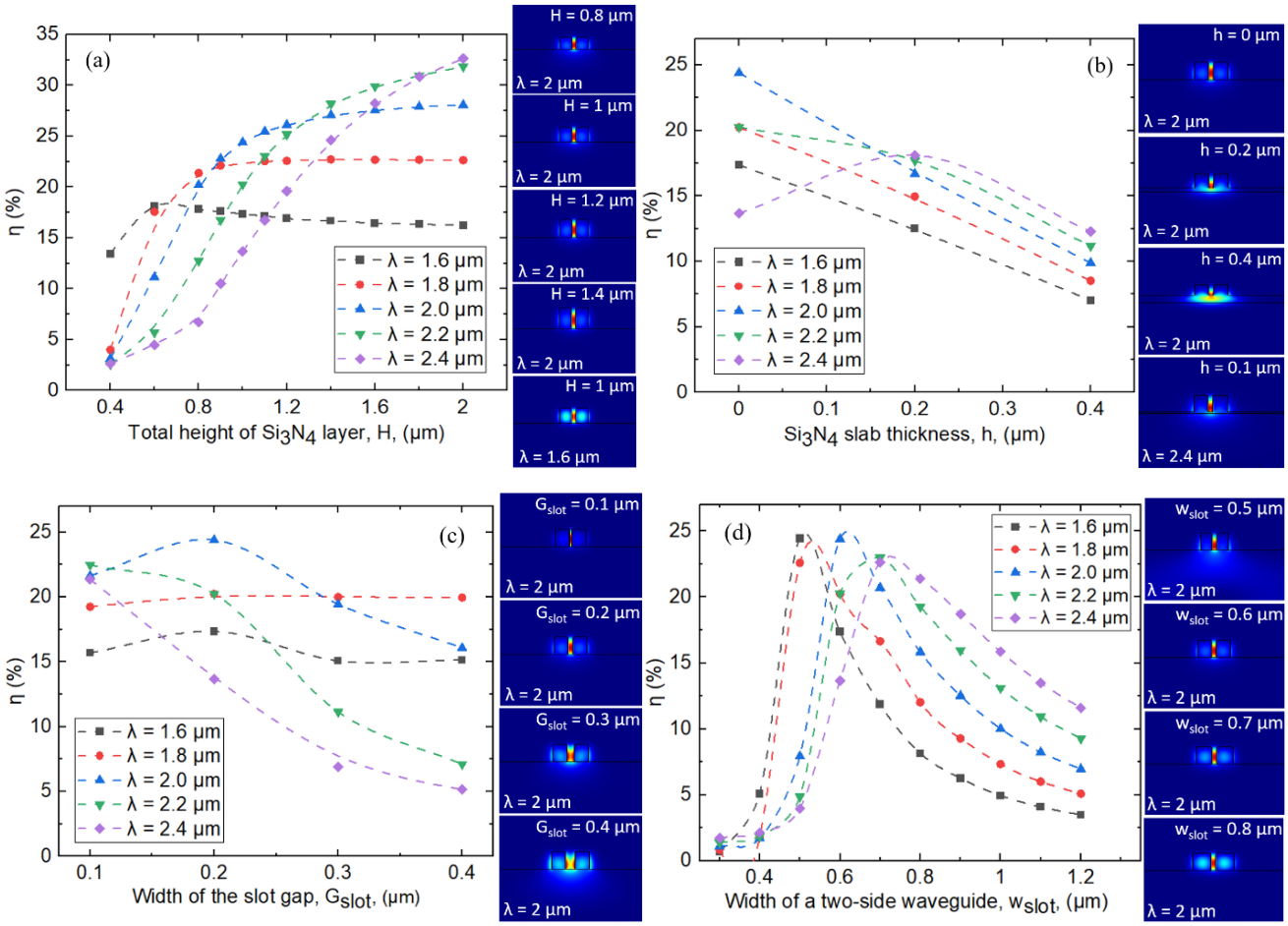

Figure 2. The ratio of the optical power in the air to the total guided optical power, η, in percentage for the slot waveguide with different (**a**) total height of the Si_3N_4 layer, H (h, G_{slot}, and w_{slot} are kept constant at 0, 0.2, and 0.6 μm), (**b**) slab thickness, h (H, G_{slot}, and w_{slot} are kept constant at 1, 0.2, and 0.6 μm), (**c**) width of the slot gap, G_{slot} (H, h, and w_{slot} are kept constant at 1, 0, and 0.6 μm), (**d**) width of a two-side waveguide, w_{slot} (H, h, and G_{slot} are kept constant at 1, 0, and 0.2 μm), at different optical wavelength values from λ = 1.6 to 2.4 μm.

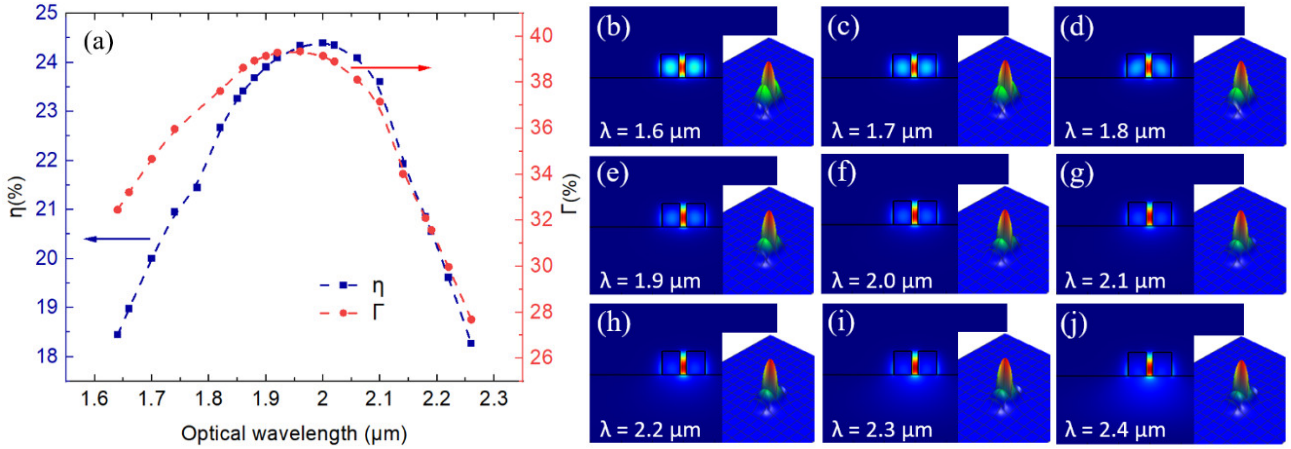

Figure 3. (**a**) Values of η and Γ of the selected Si_3N_4 slot waveguide structure with H = 1 μm, h = 0 μm, G_{slot} = 0.2 μm, and w_{slot} = 0.6 μm at different optical wavelength (λ) values. (**b**–**j**) Optical intensity of the quasi transverse-electric (TE) fundamental mode of the Si_3N_4 slot waveguide for λ from 1.6 to 2.4 μm. In the inset of Figure 3b–j, 3D mode profiles (Optiwave) of the electric field amplitude are also provided for every corresponding cross-sectional mode profile of optical intensity.

4. Si_3N_4 Multi-Mode Interferometer and Slot Waveguide for Wideband On-Chip Optical Gas Sensing

As aforementioned, we focus on employing Si_3N_4 MMI and tapering slot structures for wideband optical coupling from the Si_3N_4 strip entrance waveguide into the Si_3N_4 slot waveguide (Figure 1a) for spectroscopic sensing using absorption of gas molecules over the spectral range of interest. To identify the most appropriate structure, we proceed to optimize the Si_3N_4 MMI and tapering slot parts, and subsequently the spectral optical transmission of each optimized structure is independently investigated to verify its potential for wideband usage with respect to the identified Si_3N_4 slot waveguide. For every optimized MMI and tapering slot structure, we start the optimization process of the MMI design by choosing the width of MMI entrance (w_{in}) to be 1.4 μm. A relatively large w_{in} is typically preferred in MMI design to reduce refraction caused by a narrower entrance section, and to properly cover the entire wavelength values of interest. Later, we perform EME simulation, a proven method for the design of MMI devices and optical tapers [40], to optimize sequentially the width of MMI main waveguide (w_{mmi}), the length of MMI main waveguide (L_{mmi}), the distance between the two output waveguides (D), width of MMI output waveguide (w_{out}), the length of tapering slot parts ($L_{out,1}$ and L_{taper}). The length values of the straight section after the MMI (L_{out}) and between the two slot tapers ($L_{out,2}$) are selected to be constant at 5 μm as they are not critical parameters. w_{mmi} needs to be large enough to support enough optical modes for proper interference, L_{mmi} should be consistent with the beat length of the interference, and sufficiently large D would ensure easy fabrication of the trench between the two output waveguides. $L_{out,1}$ and L_{taper} need to be long enough to allow adiabatic transfer of the optical mode from the two MMI output waveguides to the slot waveguide via two tapering slots. Figure 4a reports intensity profile of the optical propagation inside the Si_3N_4 multi-mode interferometer and slot waveguide structure at the optical wavelength of 1.9 μm. After optimization, we arrive at w_{mmi} = 6 μm, L_{mmi} = 17 μm, D = 3 μm, w_{out} = 1.8 μm, $L_{out,1}$ = 20 μm, and L_{taper} = 80 μm. It is important to note that the tolerance of an MMI device against wavelength variation depends essentially on the width of the access waveguide, as a wider access waveguide will relax the constrain of wavelength and dimension variation before reaching a certain value of loss penalty [55]. Therefore, using a relatively wide w_{out} of 1.8 μm plays an important role in obtaining a wideband performance from the MMI. A taper structure would later decrease the width to the desired values of 0.6 μm at the slot region. As in Figure 4b (blue curve), the highest optical transmission is obtained around the optical wavelength of 1.9 μm, with an optical transmission loss of 0.23 dB (~5% optical intensity loss), and the structure is found to provide a spectral region with less than 3 dB optical transmission loss (50% optical intensity loss) for λ from 1.6 to 2.15 μm, corresponding to 3 dB optical bandwidth of 550 nm. To explicate, consistent with Figure 3b–j, the optical mode profiles of the targeted slot waveguide become significant in the two-side waveguide parts (resp. SiO_2 substrate) at the shorter (resp. longer) optical wavelength regions; hence, optical coupling condition via the MMI and tapering slot sections to the slot waveguide will become diverted from the optimized condition at the center wavelength, which is designed to project light into the optical mode at the gap part of the slot waveguide. To verify our explanation, we also investigate spectral optical transmission of the MMI and tapering slot structures optimized to obtain highest optical transmission (optical transmission loss of 0.23 dB) at the lower (resp. higher) optical wavelength value of 1.8 μm (resp. 2 μm). As in Figure 4b, despite having the center wavelength decrease (resp. increase) to 1.8 μm (resp. 2 μm) as in the green (red) curves, optical transmission loss quickly increases to 3 dB at approximately the same optical wavelength values of 1.6 μm (resp. 2.15 μm), affirming that the operating spectral range in which the proposed structure of Figure 1a can be employed for efficient wideband optical coupling is related to optical mode profiles at different optical wavelengths of the selected slot waveguide. Nevertheless, our simulation shows that the MMI and tapering slot structure can be designed to successfully cover all the usable spectral range of the slot waveguide for wideband optical sensing. With respect to the previous

works, optical loss of less than 0.45 dB (Over 90% efficiency) from the strip waveguide at the MMI entrance via Si_3N_4 MMI and tapering slot structures to the slot waveguide is maintained between 1.82 to 2 µm optical wavelengths (180-nm-wide spectral range), comparable to the previous investigation based on silicon-on-insulator (SOI) waveguide platform between 1.45 and 1.57 µm optical wavelengths (120-nm-wide spectral range) for optical interconnect application [44]. Moreover, optical transmission efficiency from the two waveguides at MMI output to the slot waveguide via the tapering waveguide part is found to be >99%, which is comparable to that reported by [42], in which its architecture on the SOI platform is based on 50/50 power splitter, instead of an MMI, focusing on the optical wavelength of 1550 nm for optical communication. Last, but not least, although direct butt coupling strategy could be used in the SOI platform between 1.45 and 1.65 µm optical wavelengths [56], in our work based on 1-µm-thick Si_3N_4 on SiO_2 waveguide platform, as in Figure 4b (gray curve) we have verified that such approach would decrease obtainable optical transmission by >1 dB around the center wavelength regions, in order to couple optical signal into the Si_3N_4 slot waveguide designed for wideband optical sensing between 1.6 and 2.2 µm optical wavelengths.

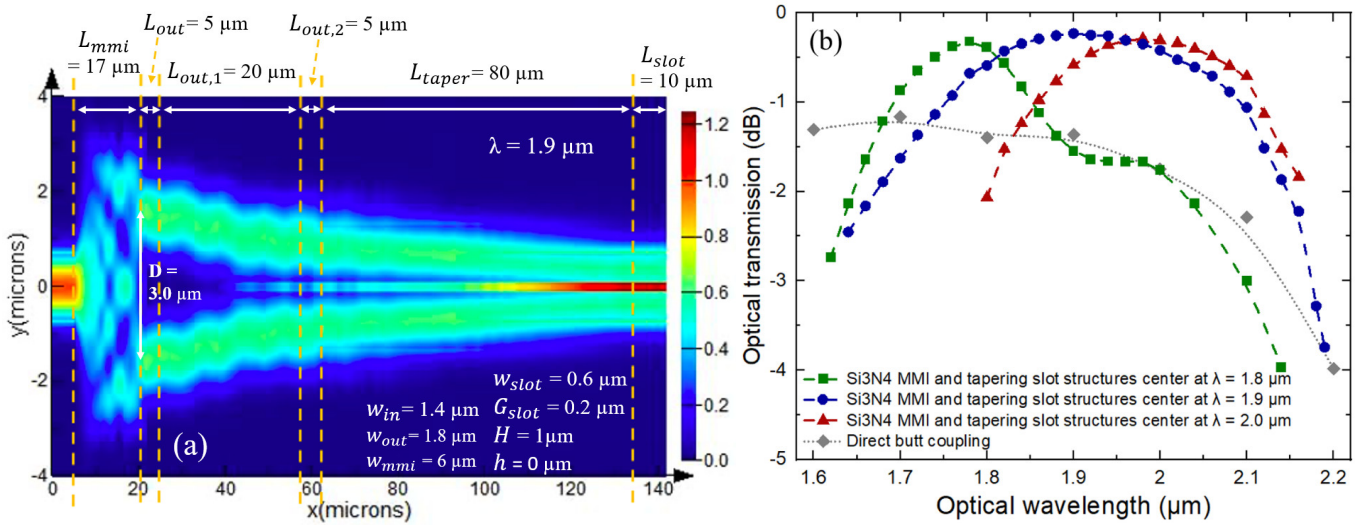

Figure 4. (**a**) Top view optical intensity profile of light propagation from a Si_3N_4 strip waveguide via the structure under investigation of a Si_3N_4 MMI and tapering slot waveguides to the straight slot waveguide at λ = 1.9 µm, for the structure optimized to have center wavelength at λ ~ 1.9 µm. (**b**) Spectral optical transmission of the MMI and tapering slot structures optimized to have center wavelength at λ ~ 1.8 (green), 1.9 (blue), and 2.0 (red) µm respectively. For the structure with the center wavelength at λ ~ 1.9 µm, an optical transmission loss of 0.23 dB (~5% optical intensity loss) with 3-dB bandwidth (<50% optical intensity loss) of 550 nm from λ = 1.6 to 2.15 µm can be obtained. The gray curve gives spectral optical transmission using direct butt coupling strategy for comparison; obtainable optical transmission decreases by >1 dB over the spectral range of interest.

To retrieve the potential of the investigated structure for optical sensing of gas molecules, we evaluated the minimum detectable concentration (C_{min}) of several important gas molecules including methane (CH_4), water vapor (H_2O), ammonia (NH_3), and carbon dioxide (CO_2), which have absorption lines within the operating bandwidth between 1.6 and 2.2 µm optical wavelengths. C_{min} of an evanescent field absorption optical sensor can be evaluated by the following expression [39,57,58]:

$$C_{min}(mol/L) = -ln\left[1 - \left\{\left(SNR \cdot NEP \cdot \sqrt{B}\right)/P_0 \exp\left(-\alpha L_{opt}\right)\right\}\right]/\varepsilon\eta L_{opt}$$

where SNR, NEP, and B stand for signal-to-noise ratio, noise equivalent power, and bandwidth of the photodetector employed in the measurement; therefore, these parameters depend critically on the performance of the detection system and operating conditions.

P_0(W) is the optical power arriving at the Si_3N_4 slot waveguide, η represents the ratio of the optical power in the air to the total guided optical power as discussed earlier, $\varepsilon(\mathrm{Lmol^{-1}cm^{-1}})$ is molar absorption of gas molecules, L_{opt} (cm) is the optimal waveguide length, and $\alpha(\mathrm{cm^{-1}})$ is the waveguide intrinsic optical loss. We used relatively typical values of SNR = 10, NEP = 5×10^{-12} W/$\sqrt{\mathrm{Hz}}$, and B = 5 kHz (0.1 ms integration time), 5 Hz (0.1 s integration time), or 0.05 Hz (10 s integration time) [4,6,18,57,58]. The value of NEP was estimated from available commercial photodetector within the optical wavelength of interest (UPD-3N(5N)-IR2-P, alphalas.com), and being conservative with respect to the number used in previous works at the longer wavelength values [18,58,59]. It is worth noting that around the 2 μm optical wavelengths, operation at room temperature is possible, and thermal noise dominates [18]. The integration time, t, can be related to the bandwidth (BW) of the photodetector as $t = 1/(2{\cdot}BW)$ [60]. Assuming optical power of 1 mW at the entrance of the MMI, P_0 arriving at the Si_3N_4 slot waveguide for each optical wavelength is then 1 mW corrected by the optical transmission spectra of the MMI and tapering slot structures obtained in Figure 4b (blue curve). α is estimated to be 2 dB/cm, which results in L_{opt} of ~2 cm [4]. Si_3N_4 was projected to be a low-loss platform at the wavelength of interest [3], and a low-loss Si_3N_4 on oxide waveguide was demonstrated up to the optical wavelength of 2.6 um (0.6 dB/cm) [35,61,62]. Therefore, an estimation of 2 dB/cm propagation loss should be considered reasonably conservative. Molar absorption values, ε, of each gas molecule are obtained from the HITRAN database and summarized in Table 1 at different optical wavelengths [63]. η values of the slot waveguide are summarized in Figure 3a. Although, as expected, the molar absorption values in this short-wave infrared region are generally lower than those in the mid-wave infrared region [39], minimum detectable concentration at ppm levels can be attained with reasonable values of integration time. These estimated detection limit values are lower than the occupational exposure limit of 1000 ppm, 25 ppm, and 5000 ppm for CH_4, NH_3, and CO_2 recommended by the international environmental standards, respectively [64]. For water vapor, the resolution limit of a few ppm already makes it compatible with the moisture level required for industrial processes [65]. Moreover, the estimated detection limit values CH_4, NH_3, and CO_2 are compatible with the concentration needed to be regulated in pig houses of ~24, ~12, and ~500 ppm, respectively, as measured by a free space configuration [66], affirming potential applications of the investigated structure. It should be noted that although the detection limit of free-space configuration will typically be lower than the waveguide one thanks to the much longer interaction length, the figure of merit when considering both the detection limit and device's compact size can be advantageous for waveguide configuration [59]. In addition, the definition of a tight slot gap should be one of the most critical steps that could affect the projected detection performance, despite significant development on etching technology to obtain vertical and smooth sidewall in Si-based devices [52–54]. Therefore, we investigate the detection performance with respect to the variation in the value of gap width at the bottom part of the slot (x) from an as-designed slot gap with vertical sidewall (x = 200 nm) to the case that the etching is significantly not completed at the bottom part of the slot (x = 25 nm), taking into account the variation in every section that has 200 nm slot gap including the $L_{out,2}$, L_{taper}, and L_{slot} regions. As in Figure 5a,b, detection performance can be maintained even though the bottom part of the slot is partially etched (x = 160, 110, and 70 nm.) Only the significant case of x = 25 nm would result in a considerable deviation of detection performance.

Table 1. Molar gas absorption data of each gas molecule with absorption lines between 1.6 and 2.2 optical wavelengths [63] and corresponding projected detection resolution.

Gas Molecules	Optical Wavelength (μm)	Molar Absorption ($Lmol^{-1}cm^{-1}$)	Estimated Detection Limit (ppm)		
			Integration Time (second)		
			0.1 ms	0.1 s	10 s
CH_4	1.65	~3.8	262	8.38	0.838
H_2O	1.85	~5.2	94.3	3.01	0.301
NH_3	1.95	~3.4	136	4.37	0.437
CO_2	2	~1.1	437	13.9	1.39

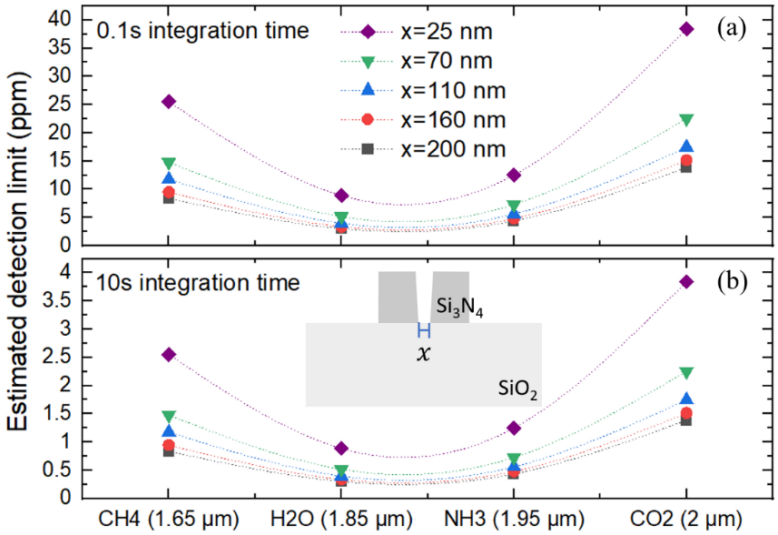

Figure 5. Detection performance with respect to the variation in the slot gap width at the bottom part of the slot (x) from an as-designed slot gap with vertical sidewall (x = 200 nm) to the case that the etching is significantly not completed at the bottom part of the slot (x = 25 nm), taking into account the variation in every section that has 200 nm slot gap including the $L_{out,2}$, L_{taper}, and L_{slot} regions. For both (**a**) 0.1 s and (**b**) 10 s integration time, detection performance can be maintained even though the bottom part of the slot is partially etched (x = 160, 110, and 70 nm). Only the significant case of x = 25 nm would result in a considerable deviation of detection performance.

5. Conclusions

The potential of Si_3N_4 on SiO_2 waveguide platform toward a wideband spectroscopic detection around the optical wavelength of 2 μm is investigated. A Si_3N_4 slot waveguide with capability to facilitate wideband on-chip spectroscopic sensing around 2 μm is identified by systematic optical mode analysis, and from EME investigation, a Si_3N_4 MMI with tapering slot waveguides can be employed for efficient optical coupling from a strip waveguide to the identified slot waveguide over its entire usable spectral range from 1.6 to 2.2 μm optical wavelengths. Optical mode profiles at different optical wavelengths of the slot waveguide would play an important role in determining the useful spectral range of the system for optical sensing based on optical absorption of the evanescent field. From the analysis, the detection limit of the investigated structure is compatible with the requirements for environmental and agricultural usages. As on-chip broadband light source and spectrometer systems [37,38] are already investigated in Si_3N_4 systems, this investigation provides further information toward the development of Si_3N_4-based on-chip spectroscopic sensing.

Author Contributions: Conceptualization, P.C. and D.M.-M.; data curation, N.K.; funding acquisition, P.C.; investigation, N.K.; methodology, N.K., P.C. and D.M.-M.; supervision, P.C., P.L., L.V. and D.M.-M.; validation, P.L., X.L.R., L.V. and D.M.-M.; writing—original draft, P.C.; writing—review and editing, N.K., P.L., X.L.R., L.V. and D.M.-M. All authors have read and agreed to the published version of the manuscript.

Funding: Kasetsart University Research and Development Institute (KURDI), National Research Council of Thailand (NRCT): NRCT5-RSA63002-05, the Capacity Building of KU Students on Internationalization Program from international affairs division, Kasetsart University.

Institutional Review Board Statement: Not applicable.

Informed Consent Statement: Not applicable.

Data Availability Statement: Not applicable.

Conflicts of Interest: The authors declare no conflict of interest.

References

1. Thomson, D.; Zilkie, A.; Bowers, J.E.; Komljenovic, T.; Reed, G.T.; Vivien, L.; Marris-Morini, D.; Cassan, E.; Virot, L.; Fédéli, J.-M.; et al. Roadmap on silicon photonics. *J. Opt.* **2016**, *18*, 073003. [CrossRef]
2. Wang, X.; Liu, J. Emerging technologies in Si active photonics. *J. Semicond.* **2018**, *39*, 061001. [CrossRef]
3. Soref, R. Mid-infrared photonics in silicon and germanium. *Nat. Photonics* **2010**, *4*, 495–497. [CrossRef]
4. Lin, H.; Luo, Z.; Gu, T.; Kimerling, L.C.; Wada, K.; Agarwal, A.; Hu, J. Mid-infrared integrated photonics on silicon: A perspective. *Nanophotonics* **2017**, *7*, 393–420. [CrossRef]
5. Wu, J.; Yue, G.; Chen, W.; Xing, Z.; Wang, J.; Wong, W.R.; Cheng, Z.; Set, S.Y.; Murugan, G.S.; Wang, X.; et al. On-Chip Optical Gas Sensors Based on Group-IV Materials. *ACS Photonics* **2020**, *7*, 2923–2940. [CrossRef]
6. Gutierrez-Arroyo, A.; Baudet, E.; Bodiou, L.; Nazabal, V.; Rinnert, E.; Michel, K.; Bureau, B.; Colas, F.; Charriera, J. Theoretical study of an evanescent optical integrated sensor for multipurpose detection of gases and liquids in the Mid-Infrared. *Sens. Actuators B Chem.* **2017**, *242*, 842–848. [CrossRef]
7. Ma, Y.; Dong, B.; Lee, C. Progress of infrared guided-wave nanophotonic sensors and devices. *Nano Converg.* **2020**, *7*, 1–34. [CrossRef] [PubMed]
8. Tombez, L.; Zhang, E.J.; Orcutt, J.S.; Kamlapurkar, S.; Green, W.M.J. Methane absorption spectroscopy on a silicon photonic chip. *Optica* **2017**, *4*, 1322–1325. [CrossRef]
9. Ranacher, C.; Consani, C.; Tortschanoff, A.; Jannesari, R.; Bergmeister, M.; Grille, T.; Jakoby, B. Mid-infrared absorption gas sensing using a silicon strip waveguide. *Sens. Actuators A Phys.* **2018**, *277*, 117–123. [CrossRef]
10. Yazici, M.S.; Dong, B.; Hasan, D.; Sun, F.; Lee, C. Integration of MEMS IR detectors with MIR waveguides for sensing applications. *Opt. Express* **2020**, *28*, 11524–11537. [CrossRef] [PubMed]
11. Consani, C.; Ranacher, C.; Tortschanoff, A.; Grille, T.; Irsigler, P.; Jakoby, B. Mid-infrared photonic gas sensing using a silicon waveguide and an integrated emitter. *Sens. Actuators B Chem.* **2018**, *274*, 60–65. [CrossRef]
12. Dong, B.; Hu, T.; Luo, X.; Chang, Y.; Guo, X.; Wang, H.; Kwong, D.-L.; Lo, G.-Q.; Lee, C. Wavelength-Flattened Directional Coupler Based Mid-Infrared Chemical Sensor Using Bragg Wavelength in Subwavelength Grating Structure. *Nanomaterials* **2018**, *8*, 893. [CrossRef]
13. Crowder, J.G.; Smith, S.D.; Vass, A.; Keddie, J. Infrared methods for gas detection. In *Mid-Infrared Semiconductor Optoelectronics*; Springer: New York, NY, USA, 2006.
14. Rogalski, A.; Chrzanowski, K. Infrared devices and techniques. *Opto Electron. Rev.* **2002**, *10*, 111–136.
15. He, L.; Guo, Y.; Han, Z.; Wada, K.; Kimerling, L.C.; Michel, J.; Agarwal, A.M.; Li, G.; Zhang, L. Loss reduction of silicon-on-insulator waveguides for deep mid-infrared applications. *Opt. Lett.* **2017**, *42*, 3454–3457. [CrossRef] [PubMed]
16. Han, Z.; Lin, P.; Singh, V.; Kimerling, L.; Hu, J.; Richardson, K.; Agarwal, A.; Tan, D.T.H. On-chip mid-infrared gas detection using chalcogenide glass waveguide. *Appl. Phys. Lett.* **2016**, *108*, 141106. [CrossRef]
17. Pi, M.; Zheng, C.; Bi, R.; Zhao, H.; Liang, L.; Zhang, Y.; Wang, Y.; Tittel, F.K. Design of a mid-infrared suspended chalcogenide/silica-on-silicon slot waveguide spectroscopic gas sensor with enhanced light-gas interaction effect. *Sens. Actuators B Chem.* **2019**, *297*, 126732. [CrossRef]
18. Huang, Y.; Kalyoncu, S.K.; Zhao, Q.; Torun, R.; Boyraz, O. Silicon-on-sapphire waveguides design for mid-IR evanescent field absorption gas sensors. *Opt. Commun.* **2014**, *313*, 186–194. [CrossRef]
19. Ramirez, J.M.; Vakarin, V.; Frigerio, J.; Chaisakul, P.; Chrastina, D.; le Roux, X.; Ballabio, A.; Vivien, L.; Isella, G.; Marris-Morini, D. Ge-rich graded-index Si1-xGex waveguides with broadband tight mode confinement and flat anomalous dispersion for nonlinear mid-infrared photonics. *Opt. Express* **2017**, *25*, 6561–6567. [CrossRef]
20. Montesinos-Ballester, M.; Liu, Q.; Vakarin, V.; Ramirez, J.M.; Alonso-Ramos, C.; le Roux, X.; Frigerio, J.; Ballabio, A.; Talamas, E.; Vivien, L.; et al. On-chip Fourier-transform spectrometer based on spatial heterodyning tuned by thermo-optic effect. *Sci. Rep.* **2019**, *9*, 14633. [CrossRef] [PubMed]

21. Osman, A.; Nedeljkovic, M.; Penades, J.S.; Wu, Y.; Qu, Z.; Khokhar, A.Z.; Debnath, K.; Mashanovich, G.Z. Suspended low-loss germanium waveguides for the longwave infrared. *Opt. Lett.* **2018**, *43*, 5997–6000. [CrossRef]
22. Hu, T.; Dong, B.; Luo, X.; Liow, T.-Y.; Song, J.; Lee, C.; Lo, G.-Q. Silicon photonic platforms for mid-infrared applications. *Photonics Res.* **2017**, *5*, 417–430. [CrossRef]
23. Roelkens, G.; Dave, U.D.; Gassenq, A.; Hattasan, N.; Hu, C.; Kuyken, B.; Leo, F.; Malik, A.; Muneeb, M.; Ryckeboer, E.; et al. Silicon-Based Photonic Integration Beyond the Telecommunication Wavelength Range. *IEEE J. Sel. Top. Quantum Electron.* **2014**, *20*, 8201511. [CrossRef]
24. Ye, N.; Gleeson, M.; Sadiq, M.; Roycroft, B.; Robert, C.; Yang, H.; Zhang, H.; Morrissey, P.; Suibhne, N.M.; Thomas, K.; et al. InP-Based active and passive components for communication systems at 2 µm. *J. Lightwave Technol.* **2015**, *33*, 971–975. [CrossRef]
25. ASE1900—Tm-Doped Fiber ASE Source, 50 mW, 1900 nm Band. Available online: https://www.thorlabs.com/thorproduct.cfm?partnumber=ASE1900 (accessed on 30 November 2020).
26. Subramanian, A.Z.; Ryckeboer, E.; Dhakal, A.; Peyskens, F.; Malik, A.; Kuyken, B.; Zhao, H.; Pathak, S.; Ruocco, A.; de Groote, A.; et al. Silicon and silicon nitride photonic circuits for spectroscopic sensing on-a-chip. *Photonics Res.* **2015**, *3*, B47–B59. [CrossRef]
27. Wang, R.; Vasiliev, A.; Muneeb, M.; Malik, A.; Sprengel, S.; Boehm, G.; Amann, M.-C.; Šimonytė, I.; Vizbaras, A.; Vizbaras, K.; et al. III–V-on-Silicon Photonic Integrated Circuits for Spectroscopic Sensing in the 2–4 µm Wavelength Range. *Sensors* **2017**, *17*, 1788. [CrossRef]
28. Wang, R.; Sprengel, S.; Vasiliev, A.; Boehm, G.; van Campenhout, J.; Lepage, G.; Verheyen, P.; Baets, R.; Amann, M.-C.; Roelkens, G. Widely tunable 2.3 µm III-V-on-silicon Vernier lasers for broadband spectroscopic sensing. *Photonics Res.* **2018**, *6*, 858–866. [CrossRef]
29. Gassenq, A.; Gencarelli, F.; van Campenhout, J.; Shimura, Y.; Loo, R.; Narcy, G.; Vincent, B.; Roelkens, G. GeSn/Ge heterostructure short-wave infrared photodetectors on silicon. *Opt. Express* **2012**, *20*, 27297–27303. [CrossRef] [PubMed]
30. Li, H.; Brouillet, J.; Salas, A.; Wang, X.; Liu, J. Low temperature growth of high crystallinity GeSn on amorphous layers for advanced optoelectronics. *Opt. Mater. Express* **2013**, *3*, 1385–1396. [CrossRef]
31. Pham, T.; Du, W.; Tran, H.; Margetis, J.; Tolle, J.; Sun, G.; Soref, R.A.; Naseem, H.A.; Li, B.; Yu, S.-Q. Systematic study of Si-based GeSn photodiodes with 2.6 µm detector cutoff for short-wave infrared detection. *Opt. Express* **2016**, *24*, 4519–4531. [CrossRef] [PubMed]
32. Wang, R.; Muneeb, M.; Sprengel, S.; Boehm, G.; Malik, A.; Baets, R.; Amann, M.-C.; Roelkens, G. III-V-on-silicon 2-µm-wavelength-range wavelength demultiplexers with heterogeneously integrated InP-based type-II photodetectors. *Opt. Express* **2016**, *24*, 8480–8490. [CrossRef]
33. Dong, P.; Hu, T.-C.; Zhang, L.; Dinu, M.; Kopf, R.; Tate, A.; Buhl, L.; Neilson, D.T.; Luo, X.; Liow, T.-Y.; et al. 1.9 µm hybrid silicon/iii-v semiconductor laser. *Electron. Lett.* **2013**, *49*, 664–666. [CrossRef]
34. Spott, A.; Davenport, M.; Peters, J.; Bovington, J.; Heck, M.J.R.; Stanton, E.J.; Vurgaftman, I.; Meyer, J.; Bowers, J. Heterogeneously integrated 2.0 µm CW hybrid silicon lasers at room temperature. *Opt. Lett.* **2015**, *40*, 1480–1483. [CrossRef]
35. Rahim, A.; Ryckeboer, E.; Subramanian, A.Z.; Clemmen, S.; Kuyken, B.; Dhakal, A.; Raza, A.; Hermans, A.; Muneeb, M.; Dhoore, S.; et al. Expanding the Silicon Photonics Portfolio with Silicon Nitride Photonic Integrated Circuits. *J. Lightwave Technol.* **2017**, *35*, 639–649. [CrossRef]
36. Kitamura, R.; Pilon, L.; Jonasz, M. Optical constants of silica glass from extreme ultraviolet to far infrared at near room temperature. *Appl. Opt.* **2016**, *46*, 8118–8133. [CrossRef]
37. Zhang, Z.; Yako, M.; Ju, K.; Kawai, N.; Chaisakul, P.; Tsuchizawa, T.; Hikita, M.; Yamada, K.; Ishikawa, Y.; Wada, K. A new material platform of Si photonics for implementing architecture of dense wavelength division multiplexing on Si bulk wafer. *Sci. Technol. Adv. Mater.* **2017**, *18*, 283–293. [CrossRef] [PubMed]
38. Martyshkin, D.; Fedorov, V.; Kesterson, T.; Vasilyev, S.; Guo, H.; Liu, J.; Weng, W.; Vodopyanov, K.; Kippenberg, T.J.; Mirov, S. Visible-near-middle infrared spanning supercontinuum generation in a silicon nitride (Si3N4) waveguide. *Opt. Mater. Express* **2019**, *9*, 2553–2559. [CrossRef]
39. Koompai, N.; Limsuwan, P.; le Roux, X.; Vivien, L.; Marris-Morini, D.; Chaisakul, P. Analysis of Si3N4 waveguides for on-chip gas sensing by optical absorption within the mid-infrared region between 2.7 and 3.4 µm. *Results Phys.* **2020**, *16*, 102957. [CrossRef]
40. Ziebell, M. Silicon Optical Transceiver for Local Access Networks. Ph.D. Thesis, Université Paris Sud—Paris XI, Orsay, France, 2013.
41. Lumerical's Tools Enable the Design of Photonic Components, Circuits, and Systems. Available online: https://www.lumerical.com (accessed on 30 November 2020).
42. Mere, V.; Kallega, R.; Selvaraja, S.K. Efficient and tunable strip-to-slot fundamental mode coupling. *Opt. Express* **2018**, *26*, 438–444. [CrossRef] [PubMed]
43. Dell'Olio, F.; Passaro, V.M.N. Optical sensing by optimized silicon slot waveguides. *Opt. Express* **2007**, *15*, 4977–4993. [CrossRef]
44. Deng, Q.; Liu, L.; Li, X.; Zhou, Z. Strip-slot waveguide mode converter based on symmetric multimode interference. *Opt. Lett.* **2014**, *39*, 5665–5668. [CrossRef]
45. Cheng, X.; Hong, J.; Spring, A.M.; Yokoyama, S. Fabrication of a high-Q factor ring resonator using LSCVD deposited Si3N4 film. *Opt. Mater. Express* **2017**, *7*, 2182–2187. [CrossRef]
46. El Dirani, H.; Casale, M.; Kerdiles, S.; Socquet-Clerc, C.; Letartre, X.; Monat, C.; Sciancalepore, C. Crack-Free Silicon-Nitride-on-Insulator nonlinear circuits for continuum generation in the C-Band. *IEEE Photonics Technol. Lett.* **2018**, *30*, 355–358. [CrossRef]

47. Almeida, V.R.; Xu, Q.; Barrios, C.A.; Lipson, M. Guiding and confining light in void nanostructure. *Opt. Lett.* **2004**, *29*, 1209–1211. [CrossRef] [PubMed]
48. Kita, D.M.; Michon, J.; Johnson, S.G.; Hu, J. Are slot and sub-wavelength grating waveguides better than strip waveguides for sensing? *Optica* **2018**, *5*, 1046–1054. [CrossRef]
49. Ottonello-Briano, F.; Errando-Herranz, C.; Rodjegard, H.; Martin, H.; Sohlstrom, H.; Gylfason, K.B. Carbon dioxide absorption spectroscopy with a mid-infrared silicon photonic waveguide. *Opt. Lett.* **2020**, *45*, 109–112. [CrossRef]
50. Ranacher, C.; Consani, C.; Vollert, N.; Tortschanoff, A.; Bergmeister, M.; Grille, T.; Jakoby, B. Characterization of evanescent field gas sensor structures based on silicon photonics. *IEEE Photonics J.* **2018**, *10*, 2700614. [CrossRef]
51. Grillot, F.; Vivien, L.; Laval, S.; Cassan, E. Propagation loss in single-mode ultrasmall square silicon-on-insulator optical waveguides. *J. Lightwave Technol.* **2006**, *24*, 891–896. [CrossRef]
52. Penadés, J.S.; Khokhar, A.Z.; Nedeljkovic, M.; Mashanovich, G.Z. Low-Loss Mid-Infrared SOI Slot Waveguides. *IEEE Photonics Technol. Lett.* **2015**, *27*, 1197–1199.
53. Penadés, J.S. Group IV Mid-Infrared Devices for Sensing. Ph.D. Thesis, University of Southampton, Southampton, UK, 2017.
54. Pfeiffer, M.H.P.; Liu, J.; Raja, A.S.; Morais, T.; Ghadiani, B.; Kippenberg, T.J. Ultra-smooth silicon nitride waveguides based on the Damascene reflow process: Fabrication and loss origins. *Optica* **2018**, *5*, 884–892. [CrossRef]
55. Soldano, L.B.; Pennings, E.C.M. Optical multi-mode interference devices based on self-imaging: Principles and applications. *J. Lightwave Technol.* **1995**, *13*, 615–627. [CrossRef]
56. Han, K.; Kim, S.; Wirth, J.; Teng, M.; Xuan, Y.; Niu, B.; Qi, M. Strip-slot direct mode coupler. *Opt. Express* **2016**, *24*, 6532–6541. [CrossRef] [PubMed]
57. Gutierrez-Arroyo, A.; Baudet, E.; Bodiou, L.; Lemaitre, J.; Hardy, I.; Faijan, F.; Bureau, B.; Nazabal, V.; Charrier, J. Optical characterization at 7.7 µm of an integrated platform based on chalcogenide waveguides for sensing applications in the mid-infrared. *Opt. Express* **2016**, *24*, 23109–23117. [CrossRef] [PubMed]
58. Liu, Q.; Ramirez, J.M.; Vakarin, V.; le Roux, X.; Ballabio, A.; Frigerio, J.; Chrastina, D.; Isella, G.; Bouville, D.; Vivien, L.; et al. Mid-infrared sensing between 5.2 and 6.6 µm wavelengths using Ge-rich SiGe waveguides. *Opt. Mater. Express* **2018**, *8*, 1305–1312. [CrossRef]
59. Pi, M.; Zheng, C.; Peng, Z.; Zhao, H.; Lang, J.; Liang, L.; Zhang, Y.; Wang, Y.; Tittel, F.K. Theoretical study of microcavity-enhanced absorption spectroscopy for mid-infrared methane detection using a chalcogenide/silica-on-fluoride horizontal slot-waveguide racetrack resonator. *Opt. Express* **2020**, *28*, 21432–21446. [CrossRef] [PubMed]
60. Mackowiak, V.; Peupelmann, J.; Ma, Y.; Gorges, A. *NEP—Noise Equivalent Power*; Techical Report; Thorlabs: Newton, NJ, USA, 2016.
61. Luke, K.; Okawachi, Y.; Lamont, M.R.E.; Gaeta, A.L.; Lipson, M. Broadband mid-infrared frequency comb generation in a Si3N4 microresonator. *Opt. Lett.* **2015**, *40*, 4823–4826. [CrossRef]
62. Muñoz, P.; Micó, G.; Bru, L.A.; Pastor, D.; Pérez, D.; Doménech, J.D.; Fernández, J.; Baños, R.; Gargallo, B.; Alemany, R.; et al. Silicon Nitride Photonic Integration Platforms for Visible, Near-Infrared and Mid-Infrared Applications. *Sensors* **2017**, *17*, 2088. [CrossRef]
63. HITRAN Database, HITRAN on the Web. Available online: http://hitran.iao.ru/molecule (accessed on 31 July 2019).
64. The National Institute for Occupational Safety and Health (NIOSH). Available online: https://www.cdc.gov/niosh (accessed on 30 November 2020).
65. Kumar, L.; Islam, T.; Mukhopadhyay, S.C. Sensitivity enhancement of a PPM level capacitive moisture sensor. *Electronics* **2017**, *6*, 41. [CrossRef]
66. Stachowiak, D.; Jaworski, P.; Krzaczek, P.; Maj, G.; Nikodem, M. Laser-Based Monitoring of CH_4, CO_2, NH_3, and H_2S in Animal Farming—System Characterization and Initial Demonstration. *Sensors* **2018**, *18*, 529. [CrossRef]